Received: 1 July 2021 | Revised: 20 September 2021 | Accepted: 29 September 2021

DOI: 10.1002/aic.17483

AIChE JOURNAL

FUTURES ISSUE: REACTION ENGINEERING, KINETICS AND CATALYSIS

Effects of surface species and homogeneous reactions on rates and selectivity in ethane oxidation on oxide catalysts

Yilang Liu[1] | Charles J. McGill[2] | William H. Green[2] | Prashant Deshlahra[1]

[1]Department of Chemical and Biological Engineering, Tufts University, Medford, Massachusetts, USA

[2]Department of Chemical Engineering, Massachusetts Institute of Technology, Cambridge, Massachusetts, USA

Correspondence
Prashant Deshlahra, Department of Chemical and Biological Engineering, Tufts University, Medford, MA 02155, USA.
Email: prashant.deshlahra@tufts.edu

Funding information
US Department of Energy, Office of Basic Energy Sciences, Division of Chemical Sciences, Geosciences, and Biosciences, Grant/Award Number: DE-SC0014901; National Science Foundation, Grant/Award Numbers: 1803798, 2034911, ACI-1548562

Abstract

Selective alkane oxidations on metal oxide catalysts involve complex mechanisms with multiple reactions in series and parallel, different types of reduced and oxidized surface species, and potential contributions from gas-phase reactions. Here, kinetics and thermodynamics of elementary steps involved in C_2H_6-O_2 reactions on SiO_2 -supported small vanadium oxide domains are determined using density functional theory. These surface reactions together with gas-phase mechanisms are incorporated in kinetic simulations to determine how surface and gaseous reactions interact and contribute to rates and selectivity. The results show that gas-phase reactions within pore volumes in contact with the catalyst contribute significantly to C_2H_6 activation rates, even at conditions where gas-phase reactions in empty volumes without catalyst are negligible. The majority of C_2H_6 activations occur on the surface, via H abstraction by vanadium oxo species present at terminal lattice oxygens. The gas-phase activations via H-abstraction by OH radicals also exhibit significant contributions. The reduced centers formed by reactions at vanadium oxo species are re-oxidized rapidly and, therefore, are present in very small concentrations at reaction conditions. The re-oxidation steps lead to the formation of HO_2 radicals and surface peroxo species that are also rapidly consumed and are present in small concentrations. The peroxo species preferentially convert C_2H_4 to its epoxide product and influence selectivity even at low concentrations. The gas-phase reactions decrease the concentrations of peroxo species and improve selectivity slightly. The effects of reaction conditions and catalyst site density provide further insights into how factors beyond conversions at lattice oxygens influence rates and selectivity in alkane oxidation reactions of significant industrial importance.

KEYWORDS
catalysis, computational chemistry (at solid surfaces), reaction kinetics

1 | INTRODUCTION

Oxidative conversions of hydrocarbons and oxygenates on reducible transition metal oxide catalysts are employed in large industrial processes for the production of valuable chemicals, and are of significant interest as alternatives to other current processes.[1–10] Ethane (C_2H_6) oxidative dehydrogenation, in particular, has attracted attention for its potential utilization of shale gas and production of ethylene, which serves as a key building block for the chemical industry.[1,11–13] Such oxidative conversions on oxides typically involve a rate-limiting C-H activation step,[14–18] but the species formed in this activation can undergo parallel reactions to desired and undesired products and

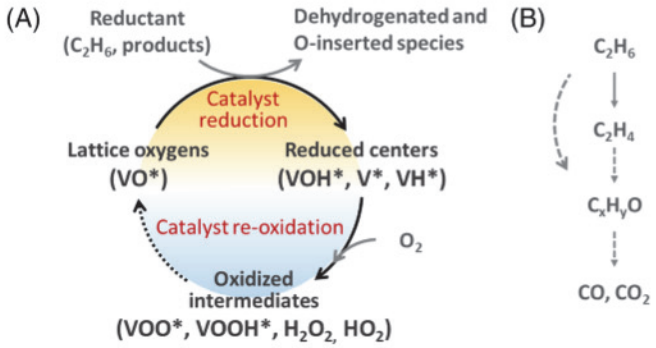

SCHEME 1 (A) Catalytic redox cycles, and (B) C_2H_6 conversions involved in C_2H_6-O_2 reactions on vanadium oxide

primary products undergo further secondary reactions.[16,19,20] These multiple cascade reactions are challenging to model in full complexity via computational methods and involve rapidly converting reactive species and intermediate products that can be inaccessible to typical experimental kinetic probes.

The oxidative conversion of alkanes on reducible metal oxide catalysts is mediated by Mars-van Krevelen redox cycles[21] such as that shown in Scheme 1. In these cycles, organic molecules reduce the catalyst by transferring H atoms or accepting O atoms leading to different types of reduced centers on the catalyst surface that are re-oxidized by O_2. For example, C_2H_6 dehydrogenation to C_2H_5 radical adds one H-atom to lattice oxygens of the oxide (VO*) leading to VOH* species (Scheme 1A). In contrast, the oxidation of the C_2H_5 radical to CH_3CHO in a single visit to the surface adds an H atom and removes an O atom leading to VH* species. The reduced centers are formed by several species mediating the sequential conversion of C_2H_6 to CO_2 (Scheme 1B). They are re-oxidized by O_2, which leads to multiple types of reactive species that further react with molecules or surface sites to form VO* species and complete catalytic turnovers (Scheme 1A). The re-oxidation steps are typically much more rapid than the reduction steps, which leads to low concentrations of the reduced centers and oxidized reactive species, making them difficult to measure using steady state kinetic and spectroscopic probes.[22] The peroxo species (VOO*) formed via the re-oxidation steps, however, have been detected in low concentrations by spectroscopy, and by employing scavenger molecules.[23–27] Computational studies have shown that VOO* species are more reactive but less selective to dehydrogenation products than VO* species.[28–30] Thus, multiple types of surface species can contribute to selectivity, and analyses must rigorously account for their concentrations and reactivity.

The redox processes involved in alkane oxidation (Scheme 1) can also form highly reactive radical and molecular species that can desorb from surfaces and undergo gas-phase reactions. In some oxide catalyst systems, mechanisms have been proposed where the formation of the alkene product occurs in the gas phase but is driven by initial C-H activation of the alkane on the surface.[11,31–34] These homogeneous pathways involving radicals prevail in relatively nonreducible catalysts that require high temperatures to activate alkanes.[35–37] Gas-phase conversions can also be promoted at moderate temperatures by incorporation of molecular species such as NO that facilitate the generation of radical species.[32,38] The involvement of the gas phase is often detected in experiments by the presence of some reactivity in empty reaction volumes at reaction temperatures. Contributions from gaseous conversions within pore volumes in contact with reducible oxide surfaces when no products are detected solely from empty volumes are not often considered. Mechanistic understanding of how the gas-phase paths influence selectivity differently under different conditions has remained unclear, leading to seemingly contradictory proposals. For example, gas-phase conversions can be responsible for high selectivity to dehydrogenated alkene products and for higher selectivity at higher oxygen pressures,[32,39] while higher O_2 pressures for reactions on reducible oxides have been proposed to decrease selectivity via homogeneous pathways.[40,41]

Here, we report detailed density functional theory (DFT) calculations and kinetic models probing sequential C_2H_6 oxidative conversions on VO_x/SiO_2 catalysts, accounting for the formation and consumption of different reduced and oxidized species involved in the redox cycles and concomitant gas-phase conversions. These calculations are performed on small cluster models previously proposed as appropriate representations of monomeric and oligomeric VO_x domains on SiO_2 support, which allowed the use of relatively high-accuracy hybrid-DFT functionals for a large number of elementary steps. The gas-phase mechanism was determined using the reaction mechanism generator (RMG) software package. Microkinetic simulations for separate surface and gas-phase reactions and combined gas-surface reactions are used to discern the contributions of different types of surface species, and of gas-phase and surface reactions to rates and selectivity.

2 | METHODS

2.1 | Catalyst models and DFT calculations for surface reactions

The SiO_2 supported vanadium oxide catalyst (VOx/SiO_2) was modeled as a V-substituted silsesquioxane cluster. Four of the eight H-SiO_3 moieties in a $H_8Si_8O_{12}$ cluster were replaced with O=VO_3 moieties to form a $H_4V_4Si_8O_{16}$ cluster, which represents a fully oxidized catalyst with vanadium-oxo species (Figure 1A). Reactions with gaseous molecules form reduced centers (Figure 1B–D) and peroxo species (Figure 1E).

Structures and energies of reactive intermediates and transition states for surface reactions involved in C_2H_6-O_2 conversions were derived from DFT calculations performed using Gaussian 09 program.[42] Hybrid B3LYP functional[43,44] and triple-ζ plus polarization basis sets (TZVP[45] and def2-TZVP[46,47]) with D3BJ empirical dispersion correction[48] and standard convergence criteria implemented within Gaussian 09 were employed for all calculations. The reported energies are for the def2-TZVP basis set. Some comparison with def2-TZVPP basis set gave energies within 1–2 kJ mol^{-1} of the

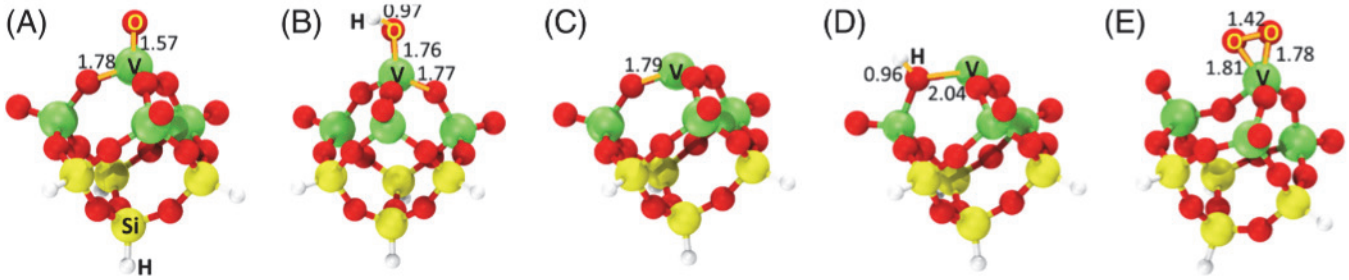

FIGURE 1 Structures of (A) vanadium-oxo species (VO*), (B–D) reduced centers (VOH*, V*, and VH*) and (E) peroxo species (VOO*) involved in C_2H_6-O_2 conversions on VO_x/SiO_2

def2-TZVP values. Transition states for surface reactions were calculated either using the quadratic synchronous transit method or using coordinate scans followed by local optimizations near maxima. The optimized structures were characterized as minima points for intermediates and saddle points for transition states by frequency calculations. The imaginary frequency for all transition states is confirmed to lie along the reaction coordinate via visual inspection, and in some cases by intrinsic reaction coordinate calculation. Atomic coordinates for these species were shown in Section S6.

Enthalpies, entropies, and Gibbs free energies were calculated from DFT-derived electronic energies and vibrational frequencies using the harmonic approximation and ideal gas statistical mechanics formalisms, as shown in Section S1.[49] Vibrational frequencies were calculated using harmonic oscillator model within Gaussian 09 at B3LYP/TZVP[45] level. The H-SiO_3 moieties were kept fixed for frequency calculations while all other atoms were relaxed. Small errors in low-frequency harmonic vibrational modes have large effects on entropy estimates. Furthermore, the harmonic approximation has been shown to be quite inaccurate for such modes, while free translators and rotors tend to be more accurate.[50] Microcalorimetry measurements have shown that a series of physisorbed molecules on oxide surfaces tend to retain 70% of changes in their gas-phase translational and rotational entropy.[51] Based on these considerations, enthalpy and entropy estimates were obtained by replacing contributions from harmonic frequencies lower than 90 cm^{-1} with a fraction (70%) of average translational and rotational contribution per mode from relevant gas-phase molecules. Illustrative examples or such replacement are provided in our recent work.[9]

2.2 | Gas-phase kinetics from reaction mechanism generator

The gas-phase kinetics for C_2H_4-O_2 reactions were derived from the reaction mechanism generator (RMG) software,[52–54] which can construct large reaction mechanisms algorithmically by applying known reaction templates to the reacting species. RMG identifies plausible reaction branches involving a species and adds a subset of these branches to the mechanism based on their predicted reactive flux in a reactor simulation. The products from added reactions are then added to the mechanism accordingly. This process is iterated until the mechanism ceases to grow. The gas-phase mechanism used in this work was generated using C_2H_6 and O_2 as the major starting species in a He gas. Minor concentrations of products and radical intermediates generated in the surface mechanism were also included: CH_3CHO, C_2H_5OH, C_2H_5OO, C_2H_5, C_2H_4, C_2H_4O (epoxide), CH_3, CH_2O, CHO, CO, HO_2, H_2O, and H_2O_2. The reactor simulation for mechanism generation was carried out as a batch reactor at 1 atm, 700–1000 K and 100 s residence time.

Thermodynamic and kinetic parameters for relevant species and reactions were extracted by RMG from libraries of the literature values. The parameters for this work originated from a mechanism for H_2-O_2 combustion from Burke et al.,[55] a mechanism for pentane ignition by Bugler et al.,[56] and a mechanism of methane combustion by Hashemi et al.[57] Forward reaction kinetics parameters absent from these three sources were estimated using reaction rate rules built from the RMG kinetics database. Reverse reaction kinetic parameters were determined using microscopic reversibility and thermodynamics parameters for species involved in the reaction. Thermodynamic parameters for species absent from the specified libraries were estimated using group additivity methods.[58]

2.3 | Cantera reactor model

The C_2H_6-O_2 reactions on VO_x/SiO_2 and in the gas phase were simulated in a series of 201 isothermal continuous stirred tank reactors used to represent a plug flow reactor within the Cantera software package.[59] The catalyst was considered as a porous bed with bed density 1 g cm^{-3}, specific surface area 100 m^2 g^{-3}, and porosity 0.796 (corresponding to 1.5 cm^3 g^{-1} pore volume and 2.6 g cm^{-3} bulk density of SiO_2). The active site density was varied between 0.1 and 10 nm^{-2}, where a site density of 0.662 nm^{-2} corresponds to 1% weight of V_2O_5 in VO_x/SiO_2 based on geometric considerations for isolated VO_x species. Rates and selectivity were determined at 700–900 K, 1–7 kPa inlet C_2H_6 and O_2 pressures and volumetric flow rates and catalyst weights adjusted to achieve desired conversions.

The rate of reaction for reaction *j* is calculated as:

$$r_j = fk\prod_i c_i^{\nu_{ij}}, \quad (1)$$

where f is the reaction symmetry factor[60–62] (details in Section S7), k is the calculated rate constant, ν_{ij} is the stoichiometric coefficient for species i in reaction j, and c_i is the concentration of a gaseous or a surface species i.

The forward rate constants (k_f) for the adsorption of gaseous species on the surface are calculated as:

$$k_f = \frac{\gamma}{\Gamma_{tot}^{m}}\sqrt{\frac{RT}{2\pi W}}, \tag{2}$$

where γ is the sticking coefficient, Γ_{tot} is the molar density of all surface sites, m is the sum of stoichiometric coefficients or all reactants, W is the molecular weight of the gas-phase species and R is the ideal gas constant. The value of γ was taken to be unity for barrierless adsorption steps. All molecular and radical species on surface can desorb via reverse of the adsorption steps. The reverse rate constants (k_r) were calculated by dividing the forward rate constants by equilibrium constants (K_c):

$$k_r = \frac{k_f}{K_c}, \tag{3}$$

$$K_c = e^{-\frac{\Delta G}{RT}}(c_{ref})^{\delta}, \tag{4}$$

where ΔG is free energy difference between products and reactants, c_{ref} is the reference concentration used for ΔG calculation (P/RT at 1 atm, 700 K), and $\delta = \sum \nu_i$ is the sum of stoichiometric coefficients or products and reactants. Surface reactions were considered to occur from adsorbed species instead of direct gas-surface reactions. The k_f and k_r values for surface reactions were determined with Eyring equation using free energy differences between transition states and precursor states. For all steps, the forward and reverse rate constants were calculated at 700, 750, 800, 850, and 900 K and the values were regressed to the following equation form:

$$k = AT^{b}e^{-E_a/RT}. \tag{5}$$

The values of constants A, b, and E_a obtained from such regression were used for simulation in Cantera.

3 | RESULTS AND DISCUSSION

3.1 | Structure of VO_x/SiO_2 and reactivity of O atoms

Figure 1 shows the structure $H_4V_4Si_8O_{16}$ V-substituted silsesquioxane cluster containing four tetrahedral O=VO_3 species with a central V atom connected to three other V atoms via V-O-V bonds. Vanadium oxide tends to exist as tetrahedral O=VO_3 vanadate species at low surface densities.[63–65] V-substituted silsesquioxane clusters have been used previously as suitable models of monovanadate species for investigating alcohol and hydrocarbon oxidations using

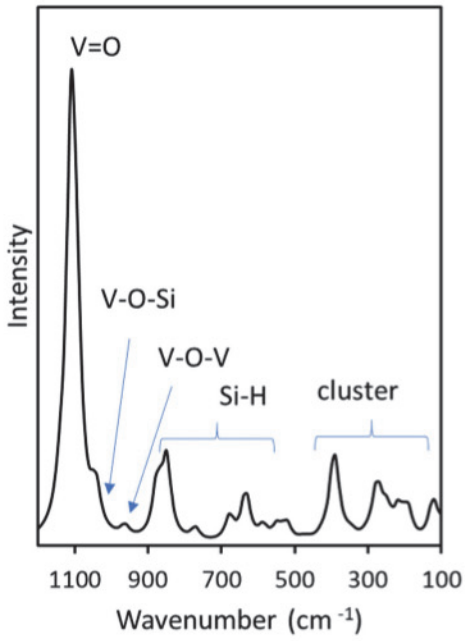

FIGURE 2 Density functional theory-derived Raman spectra of V=O* species represented by a $H_4V_4Si_8O_{16}$ cluster

DFT.[28,30,66,67] The monovanadate species, however, tend to exhibit high barriers and low reactivity for activating strong C-H bonds of alkanes. Larger VO_x domains based on such clusters can be formed using two, three, or four V atom substitutions.[67] For four V atoms, two configurations—one with all identical V atoms on the same face of the cluster connected to two other V atoms via V-O-V bond, and another with a central V-atom connected to three other V-atoms via V-O-V bonds—exhibit the same stability.[67] The latter configuration, however, is more reactive, which led us to select this more reactive configuration for C_2H_6 and O_2 activation studies shown here.

A Raman spectrum derived from vibrational frequency calculations with no fixed atoms is shown in Figure 2. Based on visualization of the frequencies, the most intense peak at 1100 cm^{-1} corresponds to V=O stretches, consistent with but slightly shifted from the intense peak at 1040 cm^{-1} found in measured spectra of low-density VO_x/SiO_2.[63] The slight shoulder at 1050 cm^{-1} corresponds to V-O-Si stretches, while and the V-O-V stretching bands at 900 cm^{-1} and are barely discernible. The bands between 900 and 600 cm^{-1} correspond to Si-H bending modes while those below 600 cm^{-1} involve multiple V, Si, and O atoms such as symmetric expansion or twisting of the cluster. These lower frequencies represent properties of the small silsesquioxane cluster employed, and not of the active sites. Measured spectra of high surface density VO_x/SiO_2 exhibit additional intense bands near 1000 and 150 cm^{-1} corresponding to bulk V_2O_5, which are absent in Figure 1. Thus, the overall spectrum appears to be consistent with low-density VO_x/SiO_2 in which only V=O stretching peaks of tetrahedral vanadates are discernible.

The reactivity of different O atom locations (V=O, V-O-V, V-O-Si, and Si-O-Si locations on the VO* cluster, Figure 1A; VOH location on a VOH* cluster, Figure 1B; and VOO location on a VOO* cluster,

TABLE 1 Density functional theory-derived energies for H atom addition at O atoms on VO_x/SiO_2 clusters (without zero-point energy corrections)

O atom site	HAE (kJ mol^{-1})
Central V=O	−284
Side V=O	−280
V-O-V	−240
V-O-Si	−226
Si-O-Si	−127
V-OH	−241
VOO	−303

Figure 1E) is probed using H-atom addition energy (HAE), which is a descriptor of the reactivity of O atoms for C-H activation.[68] O atoms with more negative HAE values tend to be more reactive for the activation of a given C-H bond. The HAE values have also been shown to correlate well with C-O formation activation energies.[69,70] The HAE values shown in Table 1 suggest that the VOO location on the VOO* cluster is the most reactive of all locations probed. The VO* clusters, however, are much more abundant than VOO* under reaction conditions. On the VO* cluster, the central V=O is more reactive than any bridging (V-O-V, V-O-Si, Si-O-Si) or corner V=O locations. The VOH species formed from the first H-atom addition to the central V=O, is less reactive than V=O. Therefore, reactions are probed at the central V=O location on the VO* sites and the VOO location on the VOO* cluster. Next, we probe detailed paths for oxidative conversion of C_2H_6 and its products on these locations.

3.2 | Oxidative conversion of C_2H_6 on VO_x/SiO_2

The oxidation of C_2H_6 on VO_x/SiO_2 catalysts involves a series of elementary reactions passing through a number of products and radical intermediates. Scheme 2 shows the sequence of molecules and radical species for which we performed DFT calculations to derive thermodynamic and kinetic parameters. The formation of these species requires reduction of the surface site either by H addition, by O or OH removal, or by a combination of such processes as shown by the arrows of different colors. On oxo sites, elementary steps for the formations of all species shown in Scheme 2 were calculated (solid arrows). On peroxo species, only C-H activation in C_2H_6, ethylene epoxidation, C-H activation in CH_3CHO and O-insertion in CH_3CO species were calculated (dotted arrows on Scheme 2). The kinetic simulations described in Section 3.3 show that only a small fraction of the surface sites exist as peroxo sites during reaction. C_2H_6 and C_2H_4 are the most abundant gaseous species that can react at minority peroxo sites. Highly reactive and more scarce species preferentially react at the more abundant oxo sites. Therefore, the skipped steps are unlikely to affect the results. This was confirmed by small effect of the exclusion of acetaldehyde and CH_3CO conversion steps on peroxo sites. The re-oxidation of VOH*, V* and VH* sites by O_2 was also calculated

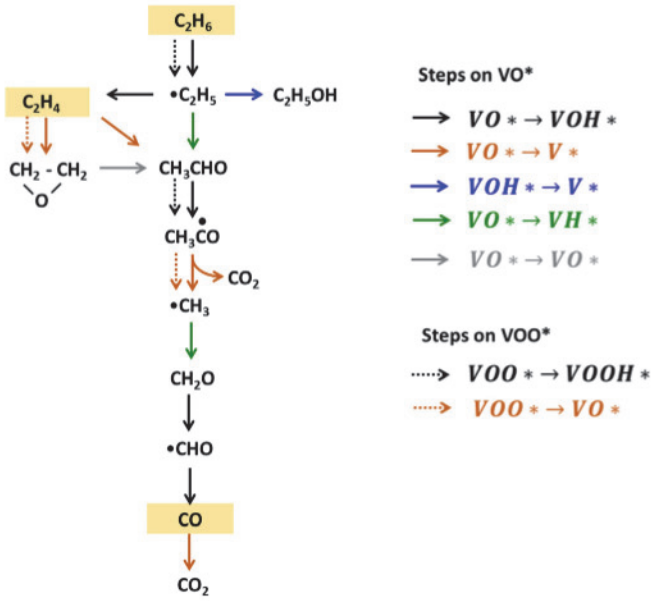

SCHEME 2 Oxidative conversion of C_2H_6 on oxide catalysts. Colors on arrows represent concomitant conversion of the surface sites as described by the legends in the right. Solid and dotted arrows represent steps on oxo (VO*) and peroxo (VOO*) sites, respectively

by DFT. All molecular and radical species formed in C_2H_6 and O_2 activations can desorb and react in the gas phase, and the gaseous products can undergo subsequent surface reactions. The kinetics of these gas-phase reactions were described by the mechanism derived from RMG comprising 164 reactions. The kinetic and thermodynamic parameters for all surface and gaseous reactions and species are provided in the Cantera input file in Section S9.

Here, we describe the free energy landscapes and structures of intermediates and transition states involved in C_2H_6 and C_2H_4 conversions on oxo sites, re-oxidation of reduced centers formed in these steps, and C_2H_6 and C_2H_4 conversions on peroxo sites. Analogous details for the subsequent conversion of C_2H_4 oxidation products are shown in the SM and briefly described here.

3.2.1 | C_2H_6 and C_2H_5 conversions on oxo sites

DFT-derived free energies of intermediates and transition states involved in C_2H_6 dehydrogenation to C_2H_5, and subsequent dehydrogenation and O-insertions leading to C_2H_4, C_2H_5OH, and CH_3CHO on a VO* cluster at 700 K and 1 atm pressure of gaseous species are shown in Figure 3. The corresponding electronic energies, enthalpies, and entropies are shown in SM (Table S2). A C-H activation in C_2H_6 forms a C_2H_5 radical and a VOH* species via a transition state with free energy of 204 kJ mol^{-1} relative to bare surface and gaseous C_2H_6 (TS01). The desorption of this C_2H_5 radical is favorable because the free energy contribution of the entropy gain from desorption is greater than that of the loss of radical-surface electronic interaction. The re-bonding of the radical with V-OH* sites to form C_2H_5OH is

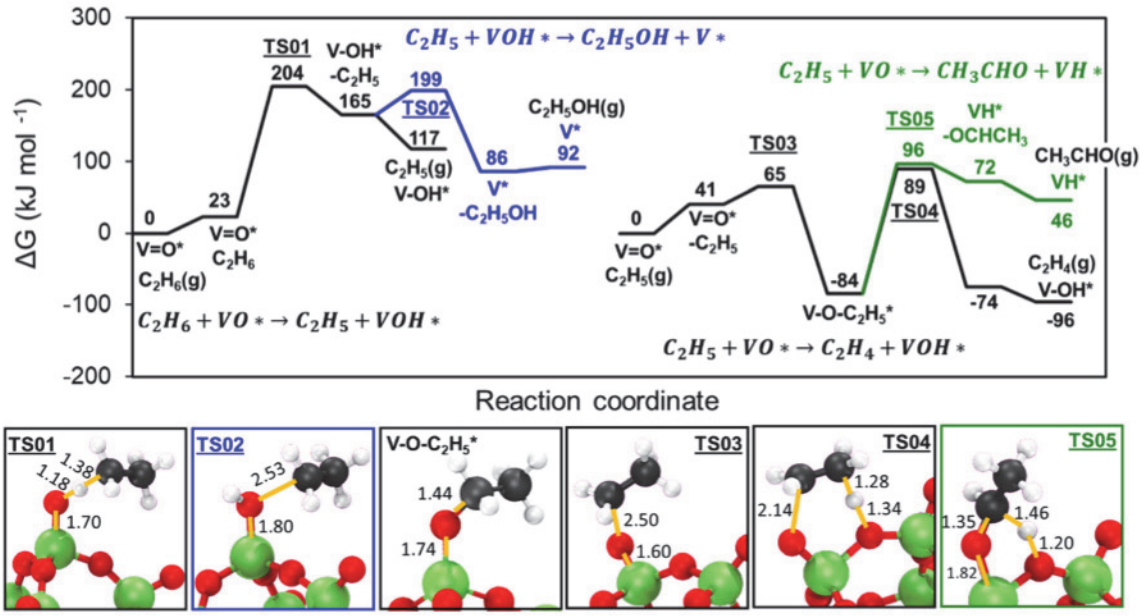

FIGURE 3 Density functional theory-derived Gibbs free energies (at 1 atm and 700 K) and structures of intermediates and transition states involved in C_2H_6 conversions to C_2H_4, C_2H_5OH and CH_3CHO on V=O*. Text and line colors correspond to arrows in Scheme 2

less favorable due to high free energy of the transition state involved ($\Delta G^{\ddagger}_{TS02}$ = 199 kJ mol^{-1}, Figure 3). Alternatively, the C_2H_5 radical can adsorb at other abundant VO* sites via C-O bond formation leading to ethoxy species (V-O-C_2H_5*), which undergoes C-H activation at the CH_3 or the CH_2 group to form the desired product C_2H_4 or the parallel CH_3CHO product, respectively. The free energy of the transition state forming C_2H_4 is slightly lower than that forming CH_3CHO ($\Delta G^{\ddagger}_{TS04}$ = 89 kJ mol^{-1} vs $\Delta G^{\ddagger}_{TS05}$ = 96 kJ mol^{-1}, Figure 3). The CH_3CHO product is also significantly less stable, which suggests greater reversibility of its formation step. These factors can lead to significant C_2H_4 selectivity at zero conversion. The relatively low barriers for C_2H_5 conversion to C_2H_4 and CH_3CHO suggests that the C-H activation in C_2H_6 forming the C_2H_5 is essentially irreversible. The barriers in Figure 3 and the electronic energies in SM (Table S2) suggest that the 4 V-atom clusters are somewhat less reactive than V_2O_5(001) surfaces reported previously,[70] but exhibit similar features reflecting irreversible C-H activation, unfavorable C_2H_5OH formation and similar barriers for C_2H_4 and CH_3CHO formation. The subsequent conversion effects not studied previously in full detail are described next.

3.2.2 | C_2H_4 conversions on oxo sites

DFT-derived free energies of intermediates and transition states for oxidations of C_2H_4 to C_2H_4O and CH_3CHO are shown in Figure 4. The corresponding electronic energies, enthalpies, and entropies are shown in SM (Table S3). C_2H_4 conversion is initiated by the formation of a bond between one C atom and the central O atom (V-OCH_2CH_2*). This species then forms a second C-O bond, leading to C_2H_4O. Alternatively, after the first C-O bond formation, the bonded C-atom undergoes a C-H bond cleavage leading to V(H)O-CH=CH_2* species followed by a C-H bond formation at the non-bonded C-atom to form CH_3CHO. The C_2H_4O (epoxide) formation path is more favorable than CH_3CHO formation ($\Delta G^{\ddagger}_{TS07}$ = 210 kJ mol^{-1} vs $\Delta G^{\ddagger}_{TS08}$ = 237 kJ mol^{-1}, Figure 4), but the desorbed C_2H_4O is much less stable leading to some reversibility of its formation. These C_2H_4 secondary reaction barriers on oxo sites are slightly higher than the primary reaction that forms C_2H_4 ($\Delta G^{\ddagger}_{TS01}$ = 204 kJ mol^{-1}, Figure 3 vs. $\Delta G^{\ddagger}_{TS07}$ = 210 kJ mol^{-1}, Figure 4), and therefore, can cause only moderate decrease selectivity with increasing conversion as more C_2H_4 accumulates.

3.2.3 | Conversions of C_2H_4O and CH_3CHO on oxo sites

Subsequent conversion of C_2H_4 oxidation products cannot directly affect C_2H_4 selectivity. However, these conversions determine how rapidly the undesired products CO and CO_2 are formed. Moreover, they can lead to the generation of species that scavenge peroxo species formed in re-oxidation or reduced clusters. Thus, they can indirectly influence selectivity, as discussed in Section 3.3. The energetics of these paths are shown in Figure S1–S3 and Tables S4–S7).

Isomerization of C_2H_4O to CH_3CHO on VO* involves a step in which a C-O bond in the epoxide breaks and a C-O bond with the surface O atom simultaneously forms via a transition state with free energy of 185 kJ mol^{-1}. This leads to the formation of a O-CH_2CH_2-O species with free energy of −24 kJ mol^{-1} (Figure S1). Further steps involve H abstraction, C-O breaking and H migration to the other C atom leading to CH_3CHO (Figure S1). The first step has the highest barrier for C_2H_4O isomerization path, and this barrier is lower than its formation from C_2H_4 sequential oxidation ($\Delta G^{\ddagger}_{TS10}$ = 185 kJ mol^{-1}, Figure S1 vs. $\Delta G^{\ddagger}_{TS07}$ = 210 kJ mol^{-1}, Figure 4).

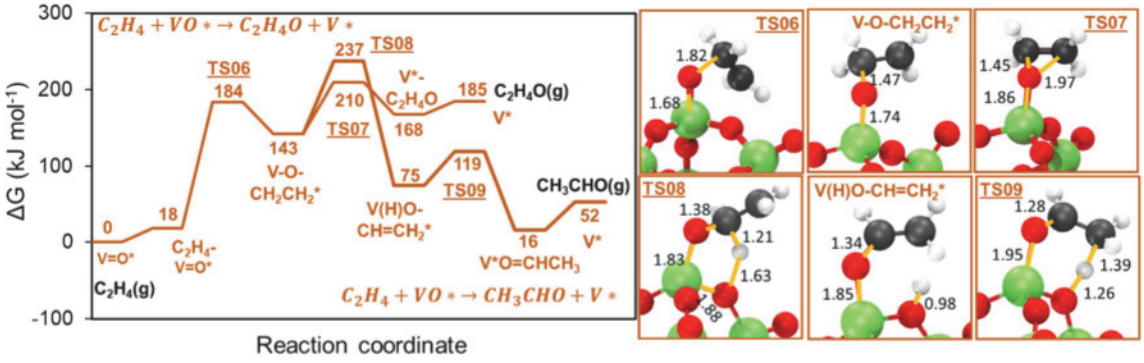

FIGURE 4 Density functional theory-derived Gibbs free energies (at 1 atm and 700 K) and structures of intermediates and transition states involved in C_2H_4 conversions to C_2H_4O (epoxide) and CH_3CHO on V=O*. Text and line colors correspond to arrows in Scheme 2

Further conversions of CH_3CHO to CO and CO_2 on V=O* site require much lower free energy barriers than previous C_2H_6 and C_2H_4 conversion steps, as shown in Figures S2 and S3. CH_3CHO is activated by C-H activation step with a transition state free energy of 161 kJ mol^{-1} (TS14, Figure S2a) leading to CH_3CO, which can desorb and bind with other V=O* sites to form acetate species. The acetate species undergo C-C cleavage forming CH_3 radical and CO_2, with a transition state with free energy 122 kJ mol^{-1} (TS15, Figure S2a). CH_3 radicals bind with V=O* to form a stable methoxy species (VO-CH_3), which undergoes a C-H activation to release CH_2O and leaving VH* as a reduced surface site. The highest energy transition state involved in this path exhibits a free energy of 101 kJ mol^{-1} (TS17, Figure S2b) and the steps are analogous to those forming CH_3CHO from C_2H_5 radicals. CH_2O undergoes two C-H activations on two V=O* sites to form CO and two V-OH* sites. The highest energy transition state in this path has a free energy 172 kJ mol^{-1} (TS18, Figure S3a). Free energy for CO oxidation transition state to form CO_2 has a high value of 235 kJ mol^{-1} (TS20, Figure S3b), suggesting CO_2 formation is not likely from CO surface oxidation.

3.2.4 | Re-oxidation of reduced VO_x/SiO_2 clusters

Reactions of C_2H_6, C_2H_4, and their products with the surface oxo sites generate reduced centers VOH*, V*, and VH* that must be re-oxidized by O_2 or species derived from O_2 to complete catalytic cycles. Figure 5 shows free energies of intermediates and transition states involved in the re-oxidation of V-OH* sites by O_2 and HO_2, and the corresponding electronic energies, enthalpies, and entropies are shown in Table S8. First, O_2 abstracts the H atom from the V-OH* site to form a V=O* and an HO_2 radical via a transition state with free energy 136 kJ mol^{-1} (TS21, Figure 5). The HO_2 radical abstracts a second H atom from another VOH* site to form either H_2O_2 and V=O*, or H_2O and VOO* via transition state with free energies 27 or 82 kJ mol^{-1}, respectively (TS23 and TS22, Figure 5). The activation energy barriers for the re-oxidation steps are much lower than C_2H_6 and C_2H_4 oxidations, suggesting re-oxidations steps are rapid and the catalyst reduction steps limit rates.

The V* and VH* species are much less stable than the VOH* species and, therefore, undergo re-oxidations with lower activation barriers, as shown in SM (Table S9). O_2 can directly bind to V* sites to form VOO* sites, in a single exothermic step. VH* site also bind with O_2 to form VHOO* in a highly exothermic step (Table S9). This species then undergoes a facile H-abstraction and forms V=O* and an OH radical. The concentrations VOO* and H_2O_2 formed in re-oxidation depend on the fraction of HO_2 species that react on reduced centers instead of reacting in the gas phase, and the rates of consumptions of these species. The re-oxidation steps also release OH radicals either on the surface or by gas-phase reactions of HO_2 and H_2O_2 species formed on the surface. The OH radicals can further re-oxidize VOH* sites leading to V=O* and H_2O via a barrierless step (Table S10). The re-oxidation of VOH* sites by H_2O_2 is mediated by a transition with free energy of 123 kJ mol^{-1} (TS24, Table S10). O atoms in the gas phase can bind to VO* sites to form peroxo species, which passes through a transition state that resembles a conversion from end-on superoxo to a peroxo bound via both O atoms with a free energy barrier of 54 kJ mol^{-1} (TS31, Table S11). The reverse of this step can release O atoms in gas-phase. The O atom can also bind to V*, VOH*, and VH* species with energetics shown in Table S11.

3.2.5 | C_2H_6 and C_2H_4 conversions on peroxo sites

Free energies of intermediates and transition states involved in C_2H_6 and C_2H_4 activations on peroxo sites formed via re-oxidation steps are shown in Figure 6, and corresponding electronic energies, enthalpies, and entropies are shown in Table S12. The transition state for the C-H activation in C_2H_6 forming C_2H_5 radical and VOOH* has a free energy of 156 kJ mol^{-1} (TS27, Figure 6). The VOOH* site formed in such C-H activations undergoes a facile conversion to V=O* and OH radicals as shown in Table S9. C_2H_4 is oxidized on VOO* by single step formation of C_2H_4O, leaving V=O* with the transition state free energy of 136 kJ mol^{-1} (TS28, Figure 6). In contrast to oxo sites, the epoxidation activation energy on peroxo site is lower than the C_2H_6 activation energy, suggesting that peroxo sites can lower the selectivity to C_2H_4 with increasing conversions by preferentially epoxidizing it. Thus, selectivity depends on the concentration of these sites and

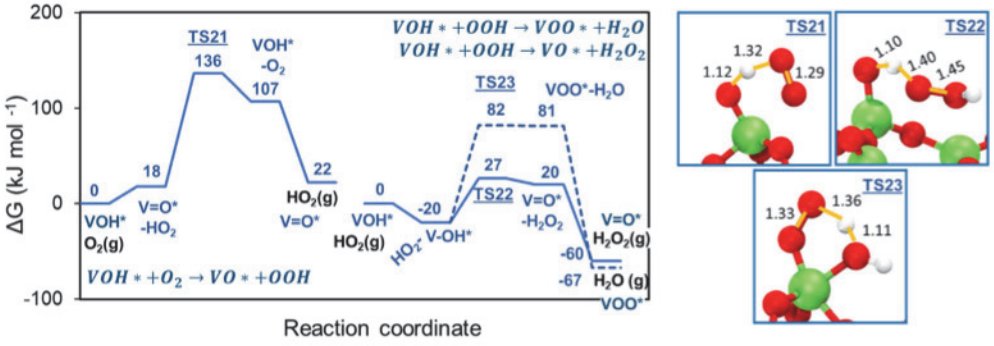

FIGURE 5 Density functional theory-derived Gibbs free energies (at 1 atm and 700 K) and structures of transition states involved in re-oxidation of VOH* by O_2 and HO_2

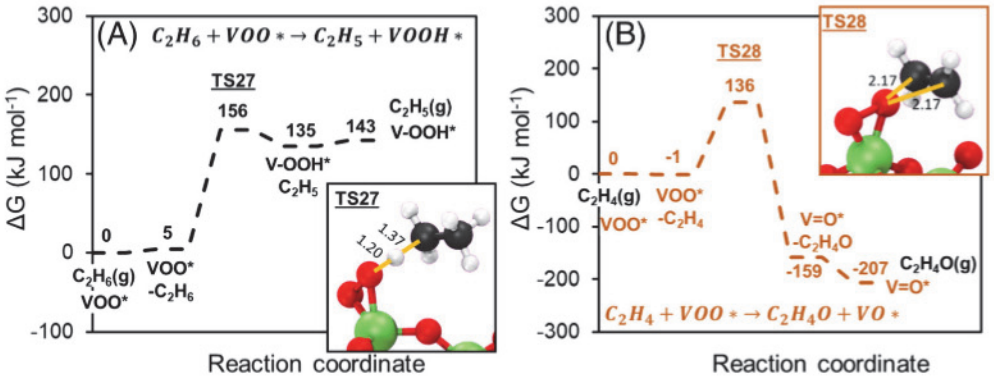

FIGURE 6 Density functional theory-derived Gibbs free energies (at 1 atm and 700 K) and structures of intermediates and transition states involved in (A) C_2H_6 and (B) C_2H_4 conversions on peroxo (VOO*) sites. Text and line colors correspond to arrows in Scheme 2

alternative paths avoiding peroxo formation or consuming peroxo can improve selectivity.

The CH_3CHO formation occurs via isomerization of C_2H_4O on abundant oxo sites (Table S4) because a species with a single C-O bond in C_2H_4 on peroxo could not be stabilized. CH_3CHO can undergo C-H activation on VOO* to form CH_3CO radical that can bind to peroxo to release CH_3 radical and CO_2 (Table S12). The free energy of the transition state for C-H activation in CH_3CHO is 127 kJ mol^{-1}, which is slightly lower than the C_2H_4 epoxidation transition state (136 kJ mol^{-1}, Figure 6), but C_2H_4 is more abundant during reaction conditions and preferentially reacts with peroxo sites.

Taken together, these DFT derived free energy profiles suggest that oxo sites are selective to C-H activation in C_2H_6 over C_2H_4 secondary oxidations, the peroxo sites are more reactive and selective to C_2H_4 epoxidation, and the re-oxidation of reduced centers can involve multiple rapid steps involving O_2, HO_2, O, and OH species. The molecular species and radical species formed in these conversions can also react further in the gas phase.

Having calculated the energetics of relevant paths for C_2H_6-O_2 reactions on VO_x/SiO_2 catalysts, we next use kinetic modeling to examine (i) how these paths together determine rates, selectivity, and surface coverages at reaction conditions, and (ii) how the surface species interact with the gas phase by releasing and accepting radical species that can drive additional gas-phase chemistry.

3.3 | Kinetic simulations

The Gibbs free energies of reactive intermediates and transition states involved in the formation of species shown in Scheme 2 were used to derive rate and equilibrium constants for the elementary steps that mediate such formations. These rate constants together with the RMG-derived rate and equilibrium constants for the homogeneous gas-phase reactions are incorporated within kinetic simulations to understand how conversions on different surface sites (V=O* and VOO*) and in gas phase couple to determine the overall rates and selectivity.

3.3.1 | Effect of gas-phase reactions on rate and selectivity

The rates of surface and gas-phase reactions are integrated along a PFR to determine changes in concentrations of reactant, products, and reactive intermediates. The C_2H_6 conversion and the selectivity to C_2H_4 at 700 K are shown in Figure 7. The conversion is negligible when only gas-phase reactions occur within the volume equivalent to the pore volume of 2 g of catalyst without any surface reactions (Figure 7A). When only the surface reactions are included in the reactor model, the conversion increases linearly along the reactor at low conversion values (indicating constant C_2H_6 activation rate) and becomes slightly sublinear at higher conversions due to the depletion of the reactants (Figure 7A). When both surface and gas-phase reactions are included, however, the conversion increases more rapidly than that for surface reactions alone (Figure 7A, approximately 26% and 31% conversion at 2 g for surface only and gas + surface, respectively). This suggests that gas-phase species contribute significantly to C_2H_6 activations, but these activations cannot be initiated within the small empty pore volume if the surface reactions do not generate the reactive species first.

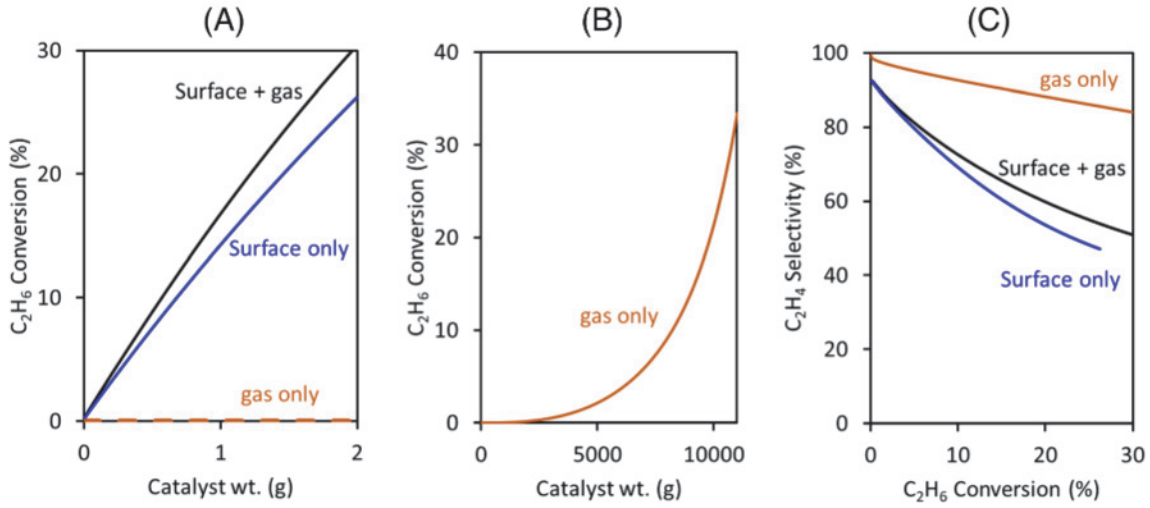

FIGURE 7 (A, B) C_2H_6 conversion as a function of catalyst weight and (C) C_2H_4 selectivity as a function of conversion for C_2H_6-O_2 reactions on VO_x/SiO_2 surface, in gas phase within catalyst pore volume, and in combined surface and gaseous reactions (700 K, 150 cm^3min^{-1}, 1 site nm^{-2}, 3 kPa C_2H_6, 3 kPa O_2). For gas-only reactions catalyst weight is used as a surrogate for the reaction volume equivalent to catalyst pore volume

When gas-phase reactions are allowed to occur within much larger volumes, the conversion increases supralinearly with volume indicating that the C_2H_6 activation rate increases with residence time (Figure 7B; reaction volume is the pore volume of the catalyst equivalent inert powder). This nonlinear increase is typical of autocatalytic gas-phase alkane oxidation reactions,[32] and it indicates that radical species generated in initial reactions lead to more facile activation of strong C-H bonds in alkane, and the oxidation products in turn generates additional reactive radicals. When the catalyst is present (Figure 7A), however, the radical species can be generated a much shorter residence times and equilibrate with surface species. As a result, conversion increase linearly with catalyst weight (or catalyst contact time), showing trends analogous to the case where all reactions occur only on the surface, and distinct from the gas-only reactions. Thus, solely comparing measurements in a small empty volume and with catalyst may lead one to conclude that gas-phase reactions are insignificant. The simulations show, however, that C_2H_6 conversion increases by 16% when gas-phase contributions are incorporated.

Figure 7C shows that C_2H_4 selectivity is higher when reactions occur only in gas phase than when they occur only on the surface. When both gas and surface reactions occur simultaneously, the C_2H_4 selectivity is in between the two cases at the conditions shown. These results suggest that gas-phase reactions can be selective towards alkene formation, which is consistent with measurements of gaseous CH_4-O_2 and C_3H_8-O_2 reactions where NO_x is used to generate radical species to initiate gas-phase chemistry at moderate temperatures,[32,38] and with systems that employ surface-mediated radical generation for selective oxidation.[36,37] The measured C_2H_4 selectivity for supported vanadium oxide catalyst at 1% conversion was found to be near 50–60% at 698–733 K,[70] which is lower than the 80–90% initial selectivity shown in Figure 7C. These differences result from a slightly higher transition state free energy for parallel conversion of C_2H_5 radical to undesired products (89 kJ mol^{-1} for TS04 vs. 96 kJ mol^{-1} for TS05 in Figure 3). These barrier differences are near zero in interpretations of measured data, which leads to near 50% selectivity. Such small differences are within the errors expected from simplified catalyst models and from limitations of DFT functionals. The qualitative trend of higher measured selectivity in gas-phase reactions[32] than reactions on supported vanadium oxide catalysts[20,70] is consistent with the simulation results shown here.

Figure 8 compares selectivity to products other than C_2H_4 for combined surface-gas reactions and with that for surface-only reactions. The results show that the most significant effect of the incorporation of gas-phase reaction is the decrease in C_2H_4O (epoxide) and CO_2 selectivity and a lesser increase in CO selectivity, which led to an overall slight increase in C_2H_4 selectivity in Figure 7C. The epoxide and CO_2 products can be preferentially produced on surface peroxo sites by reacting C_2H_4 and CH_3CO, respectively (Scheme 2). Thus, the results suggest that gas-phase conversions provide alternate paths that bypass peroxo formations and decrease peroxo species concentration to enhance selectivity. The gas-phase conversions also decrease CO_2 selectivity by dissociating CH_3CO species to CH_3 and CO, instead of converting it to CH_3 and CO_2 on peroxo sites. The formation of CO as the most significant byproduct after accounting for the interaction with the gas-phase chemistry is consistent with measurements on supported vanadium oxide catalysts in which CO selectivity is about four times the CO_2 selectivity. The simulation results in Figure 8A show approximately 5% selectivity to the epoxide product (C_2H_4O) even after incorporating gas-phase chemistry. This product is not observed in significant concentrations in measurements,[20] suggesting that the lower peroxo coverages obtained in combined surface + gas reactions or the barriers of C_2H_4O formation or its rapid consumption are somewhat inconsistent between experiment and

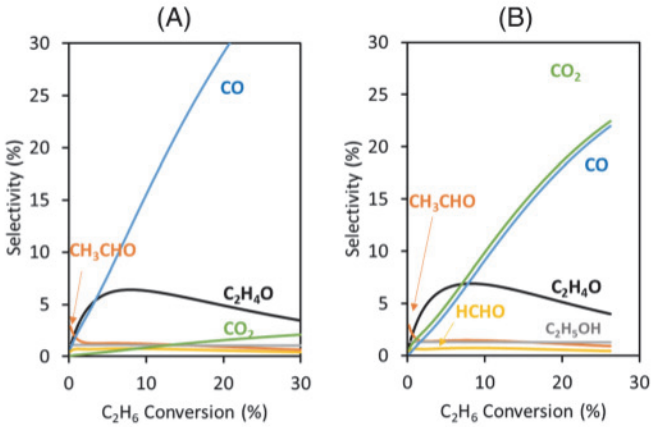

FIGURE 8 Selectivity to minor products as a function of C_2H_6 conversion as for C_2H_6-O_2 reactions when (A) both surface and gas-phase conversions are considered, and (B) when only surface conversions are considered (700 K, 1 site nm^{-2}, 150 cm^3min^{-1}, 3 kPa C_2H_6, 3 kPa O_2)

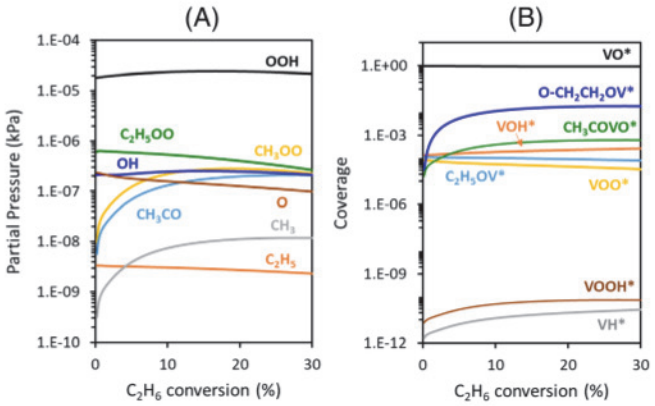

FIGURE 9 (A) Concentrations of gaseous radical species, (B) coverage of surface species along the reactor as a function of C_2H_6 conversion for combined surface and gas-phase C_2H_6-O_2 reactions (700 K, 1 site nm^{-2}, 150 cm^3min^{-1}, 3 kPa C_2H_6, 3 kPa O_2)

simulation. Catalyst supports and silanol groups may also contribute significantly to the isomerization of the epoxide.[71]

The comparison of gas and surface conversions and selectivities suggest that gas phase can, in contact with the catalyst, (i) enhance C_2H_6 activation, and (ii) slightly suppress reactions that occur on peroxo sites. Next, we examine the concentrations of different gaseous and surface reactive species and relative rates of gas and surface reactions to further probe the origins of these effects.

3.3.2 | Concentrations of gaseous and bound reactive intermediates

Figure 9 shows gaseous radical species and surface species along the reactor under combined gas and surface reactions. The radical species are present in small concentrations, consistent with their unstable nature. The HO_2 radicals, primarily formed via the abstraction of H atom at VOH* species by O_2 in the re-oxidation process, are the most abundant gaseous radical species (Figure 9A). OH radicals, O atoms, and C_2H_5OO, CH_3OO and CH_3CO radicals also have significant abundance. The OH radicals formed in this process are known to be strong and selective abstractors of H-atoms, which can contribute significantly to C_2H_6 activation.[32,38,72] The O atoms are released from surface by the cleavage of peroxo species and by gas-phase steps. The C_2H_5OO and CH_3OO radicals are formed by reaction of alkyl radicals with O_2 in the gas phase.

The surface coverage of VO* species is nearly 100% (Figure 9B), which is consistent with low free energy barriers for the re-oxidation of reduced clusters. The most abundant reduced centers are VOH* species, which have about four orders of magnitude smaller surface coverage than VO*. The surface peroxo species formed via re-oxidation steps (VOO*) have about threefold smaller coverage than the VOH* species. The low concentration of bound peroxo reflects high reactivity of these species, which leads to its rapid conversion via reaction with C_2H_4 (epoxidation) and release of O atoms in the gas phase. The coverages of other reduced centers V* and VH* and of surface VOOH* are even smaller. Bound epoxide species ($OCH_2CH_2OV^*$) exhibits higher coverage than VOH*, while ethoxy species ($C_2H_5OV^*$) and acetate species (CH_3OCOV^*) also exhibit concentrations similar to VOH* species and greater than peroxo species.

3.3.3 | Rates of gaseous and surface reactions

Figure 10 shows rates (net fluxes given by difference between forward and reverse rates) for parallel surface and gaseous reaction branches (normalized by catalyst weight for both cases) that account for the activation of C_2H_6, C_2H_5, C_2H_4, HO_2, O, and OH species for reactor model involving simultaneous gaseous and surface conversions. The rate of C_2H_6 activation at VO* sites is about six times higher than that in the gas phase via reaction with OH radicals, suggesting that both conversions have significant contributions (Figure 10A). Other C_2H_6 activation paths involving gaseous reactions with O atoms and HO_2 radicals and surface reactions with VOO* sites have much smaller contributions.

The C_2H_5 radicals predominantly react at VO* sites to form C_2H_4 (Figure 10B). Other reactions of C_2H_5 at VO* and VOH* sites, forming CH_3CHO and C_2H_5OH, respectively, have one to two orders of magnitude lower rates than C_2H_4 formation, which is consistent with selectivities near 90% at zero conversion in Figure 7C. The C_2H_5 radicals also react with O_2 in the gas phase to form C_2H_4 and HO_2. This step is more than three orders of magnitude smaller than the C_2H_4 formation step on the surface (Figure 10B). The ratio of the rate of the gas-phase step to the surface step depends not only on O_2 pressure but also on the sizes of the pores of the catalyst. Narrow pores would allow greater opportunities for collision with the walls and further enhance surface reactions. The gas-phase step is much more significant for driving the chemistry when oxide surfaces are not involved, and lead to HO_2 radicals that

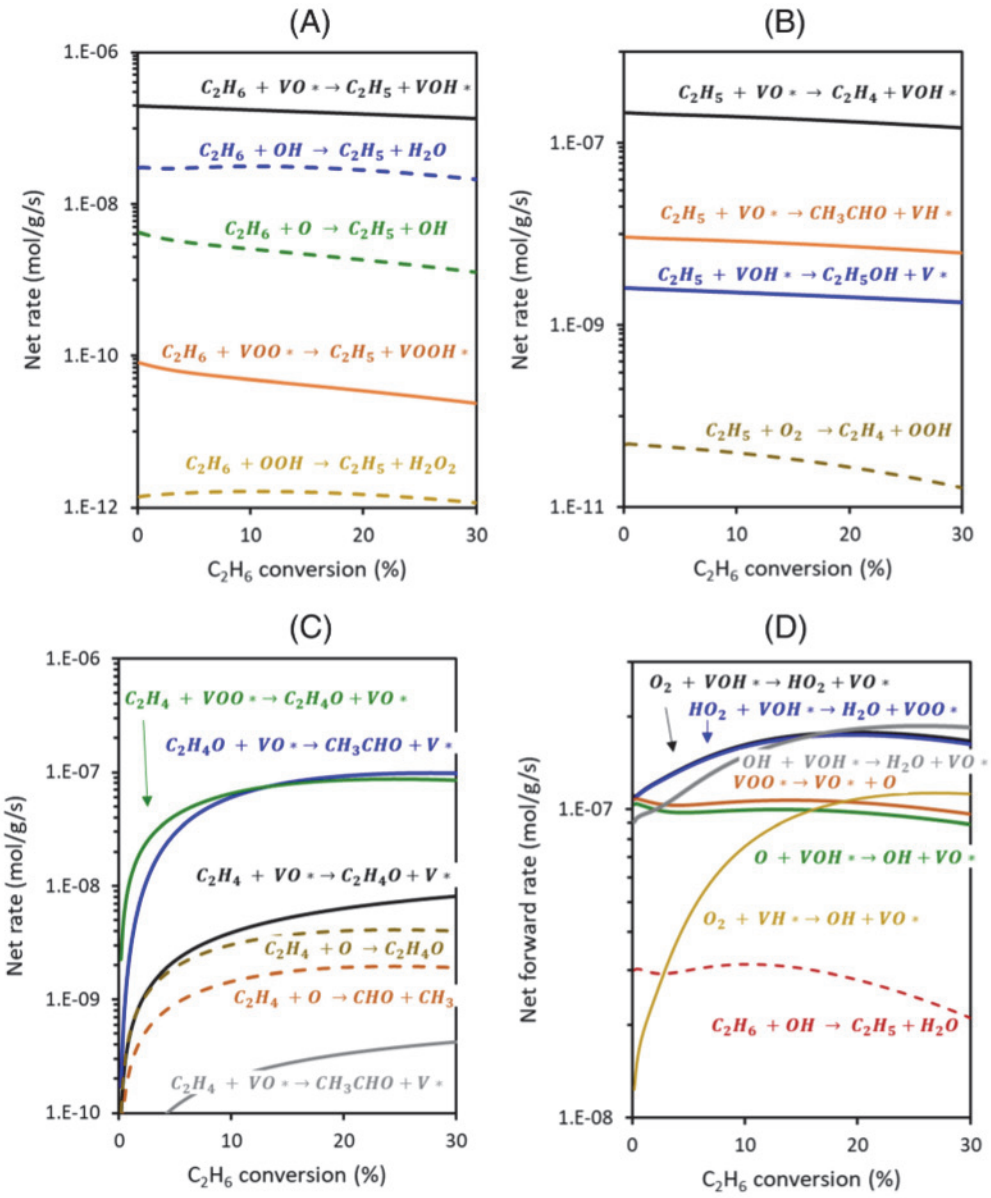

FIGURE 10 Rates of reactions that account for most of the conversions of (A) C_2H_6, (B) C_2H_5 radicals and (C) C_2H_4 as a function of C_2H_6 conversion for combined surface and gas-phase C_2H_6-O_2 reactions (700 K, 1 site nm^{-2}, 150 cm^3min^{-1}, 3 kPa C_2H_6, 3 kPa O_2). Solid and dashed lines reflect surface and gaseous reactions, respectively

eventually form OH radicals by combining with other HO_2 radicals. In this work, however, the more significant route for HO_2 generation is through the re-oxidation of surface VOH* species by O_2. The rate of gas-phase reaction between C_2H_5 and O_2 shown in Figure 10B includes contributions from two channels, one involving direct H-abstraction by O_2 and another mediated by the C_2H_5OO intermediate.[73,74] The rate C_2H_5OO channel contributed to about 30% of C_2H_5-O_2 reactions, and about 90% of C_2H_5OO species led to C_2H_4 while the remaining species formed oxygenates such as C_2H_4O.

The most significant conversion of C_2H_4 involves surface epoxidation at and VOO* sites (Figure 10C). This is consistent with the low epoxidation barriers and strong preference for epoxidation over C-H activation in Figure 6. The isomerization of the epoxide to CH_3CHO also occurs at similar rates as the epoxide formation (Figure 10C). The rates of C_2H_4 epoxidation at oxo sites and in the gas phase are also significant but smaller than the epoxidation on peroxo sites by over an order of magnitude.

Figure 10D shows the rates of different steps involving the generation and consumption of HO_2, O, and OH radicals via the re-oxidation steps. O_2 molecules are primarily activated at VOH* species to form HO_2 and VO* species. The resulting HO_2 species further react with VOH* species to form surface peroxides and H_2O, despite the fact that parallel HO_2 + VOH* reactions forming H_2O_2 have lower barrier. This is because the H_2O_2 product (despite lower barrier) is less stable and the forward and reverse rates for its formation are in equilibrium, leading to small net rates (reversibility of steps shown in Table S13 and Figure S11). The VOO* species formed by HO_2 activation at VOH* can release O atoms that react with other VOH* species for generate VO* and OH radicals. The OH radicals can then recombine with VOH* species to form H_2O or abstract H atom to form C_2H_6. Taken together, these data show that reactive species generated

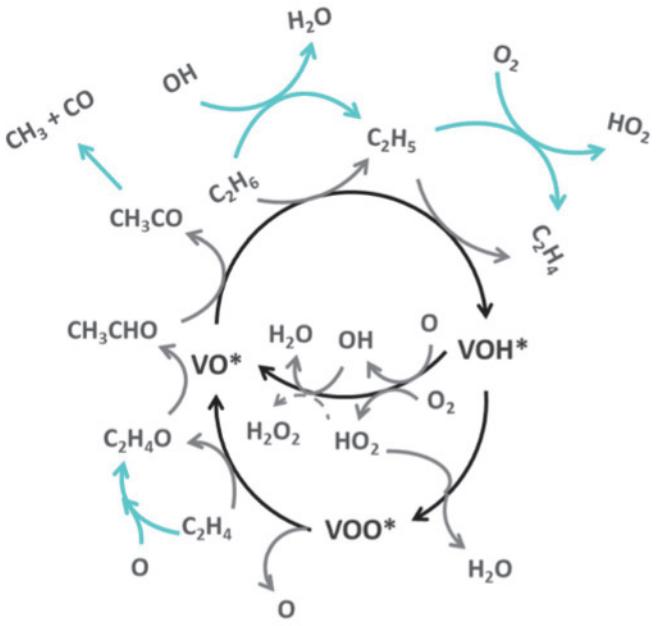

SCHEME 3 Most significant surface and gas-phase steps involved in C_2H_6-O_2 reactions, based on the rates determined from kinetic simulation results shown in Figure 10. The gas-phase steps are shown in cyan color

by initial O_2 activation can further react with reduced centers in multiple steps to eventually form H_2O. This is accompanied by significant C_2H_6 activation by OH. Other gas-phase reactions such as OH radical formation by O-donation by HO_2 to alkyl species, and by H_2O_2 cleavage also occur but are less significant than the surface mediated OH radical generation in Figure 10D. The most significant surface and gas-phase reaction in the first few steps of sequential C_2H_6 oxidation and in the re-oxidation and reactive oxygen generation steps are shown in Scheme 3. These reactions give an overall picture of how the surface and gas-phase step interact.

We also examined the effects site density, reaction temperature, C_2H_6 pressure, and O_2 pressure on rates and selectivity. These data are shown in Section S8. Increasing the site density decreases the gas-phase contribution to C_2H_6 conversion but maintained significant contribution even at 10 times greater site density than that in Figure 7 (Figure S7). Lower site densities show increased gas-phase contribution to rates and increased C_2H_4 selectivity because more gas-phase volume is available par site (Figures S7 and S8).

Temperature affects the rate very significantly, consistent with the high activation energy for C-H bond cleavage in C_2H_6 (Figure S8). The activation enthalpy derived from the temperature effects of overall C_2H_6 activation rate is 131 kJ mol^{-1}, which is similar to the enthalpy of 128 kJ mol^{-1} in Table S2. These predicted activation enthalpies are slightly higher than the 105 ± 15 kJ mol^{-1} for measurement on low surface density (11 wt. %) VO_x on SiO_2.[19] The predicted rate form the current simulation at 648 K and 3 kPa C_2H_6 is 5×10^{-5} (mol C_2H_6 [mol V s]$^{-1}$), which is about an order of magnitude higher than the measurements on 11%VO_x/SiO_2.[19] These comparisons highlight differences between measurements and simulation, but the differences can be considered small given the uncertainty in catalyst models and DFT energies.

C_2H_6 activation rates are nearly first order in C_2H_6 pressure and zero order in O_2 pressure, which is consistent with measured reaction orders.[20] The zero-order O_2 pressure dependence results from the high free energy barrier for the initial C-H activation (204 kJ mol^{-1}, Figure 3, TS01), and low barriers for the rapid re-oxidation steps (136 kJ mol^{-1}, Figure 5, TS21), which agrees well with negligible concentrations of reduced centers in Figure 9B causing nearly all lattice oxygen sites to be available for activating C_2H_6 at all O_2 pressures considered. The selectivities are insensitive to C_2H_6 pressure and decrease slightly with O_2 pressure (due to increased surface peroxo and gaseous O atom mediated reactions; Figures S9 and S10), which is also consistent with measured trends.[70]

The results described here show that (i) gaseous reactions can contribute significantly to oxidative dehydrogenation reactions even at moderate temperature, (ii) these contributions are present even when the kinetic orders are consistent with surface-only reactions and blank reactor volumes show negligible activity, and (iii) such paths can improve selectivity to C_2H_4 at some conditions by decreasing concentrations of peroxo species. We also clarify that the general pathways through gas and surface reactions interact, despite the results being specific to the catalyst model employed and its specific reactive properties. The results are expected to change with catalyst type but to involve analogous steps. The model used here involves small isolated VO_x domains that prefer to undergo-one electron reduction forming VOH* species that generate HO_2 species. Other catalysts may prefer OH pairs and O vacancies and quench radicals more efficiently.

4 | CONCLUSIONS

Alkane activations on transition metal oxides involve a complex network of reactions with many rapid steps after an initial C-H bond activation that is often rate-limiting. DFT-based computational modeling of such systems fully accounting for all steps are challenging and often such studies seek to model only the primary dehydrogenation reactions. When selectivity limitations are probed by computation, only limited parallel reaction branches and the first step in the conversion of the primary product, solely on the lattice oxygens, are considered. This work combines detailed DFT calculations for reaction branches on multiple types of surface species for C_2H_6-O_2 reactions on a small cluster model of VO_x/SiO_2 catalyst with gas-phase mechanisms and kinetic modeling to probe the extent to which such factors influence rates and selectivity.

The initial catalyst contains solely lattice O atoms on fully oxidized VO_x domains with terminal V=O species (oxo sites or VO* sites) as the most reactive location for the reactions. Organic molecules react at these sites to form gaseous radical intermediates and products, and reduced centers. The re-oxidation of the reduced centers by O_2 produces HO_2 radicals, H_2O_2, and surface peroxo species (VOO*) and further gaseous and surface steps produce OH radicals and

gaseous O atoms in small concentrations. The barriers for primary and secondary reactions on oxo and peroxo sites show that peroxo sites are less selective to oxidative dehydrogenation products and preferentially epoxidize from C_2H_4. In spite of the low concentrations, the gaseous reactions and surface peroxo sites contribute significantly to overall rate and selectivity. The gas-phase mechanisms increase rates via H atom abstraction from C_2H_6 by OH radicals. They also improve selectivity at certain conditions by generating alternate paths that decrease the surface coverage of peroxo species. These insights provide a comprehensive picture of factors beyond the properties of initial lattice oxygens that influence selectivity on oxidative dehydrogenations and related reactions on oxides.

ACKNOWLEDGMENTS

We thank Prof. Nathaniel Eagan (Tufts University) for helpful discussions and insights on details of kinetic simulations. Financial support from National Science Foundation (award numbers 1803798 and 1803343), and computational resources from Extreme Science and Engineering Discovery Environment (XSEDE),[75] supported by National Science Foundation (grant number ACI-1548562), are gratefully acknowledged. Charles J. McGill and William H. Green acknowledge support from Gas Phase Chemical Physics Program of the US Department of Energy, Office of Basic Energy Sciences, Division of Chemical Sciences, Geosciences, and Biosciences (under Award number DE-SC0014901).

AUTHOR CONTRIBUTIONS

Yilang Liu: Conceptualization (equal); data curation (equal); formal analysis (equal); investigation (equal); methodology (equal); validation (equal); visualization (equal); writing – original draft (equal); writing – review and editing (equal). **Charles McGill:** Conceptualization (equal); data curation (equal); formal analysis (equal); investigation (equal); methodology (equal); resources (equal); validation (equal); writing – original draft (equal); writing – review and editing (equal). **William Green:** Conceptualization (equal); funding acquisition (equal); methodology (equal); project administration (equal); resources (equal); software (equal); supervision (equal); writing – review and editing (equal). **Prashant Deshlahra:** Conceptualization (equal); data curation (equal); formal analysis (equal); funding acquisition (equal); investigation (equal); methodology (equal); project administration (equal); supervision (equal); writing – original draft (equal); writing – review and editing (equal).

DATA AVAILABILITY STATEMENT

The data that support the findings of this study are available from the corresponding author upon reasonable request.

ORCID

William H. Green https://orcid.org/0000-0003-2603-9694
Prashant Deshlahra https://orcid.org/0000-0002-1063-4379

REFERENCES

1. Cavani F, Ballarini N, Cericola A. Oxidative dehydrogenation of ethane and propane: how far from commercial implementation? *Catal Today*. 2007;127(1–4):113-131.
2. Batiot C, Hodnett B. The role of reactant and product bond energies in determining limitations to selective catalytic oxidations. *Appl Catal A*. 1996;137(1):179-191.
3. Getsoian AB, Shapovalov V, Bell AT. DFT+ U investigation of propene oxidation over bismuth molybdate: active sites, reaction intermediates, and the role of bismuth. *J Phys Chem C*. 2013;117(14):7123-7137.
4. Bui L, Bhan A. A kinetic model for propylene oxidation on a mixed metal oxide catalyst. *Appl Catal A*. 2018;564:1-12.
5. Melzer D, Mestl G, Wanninger K, et al. Design and synthesis of highly active MoVTeNb-oxides for ethane oxidative dehydrogenation. *Nat Commun*. 2019;10(1):1-9.
6. Hutchings GJ, Kiely CJ, Sananes-Schulz MT, Burrows A, Volta JC. Comments on the nature of the active site of vanadium phosphate catalysts for butane oxidation. *Catal Today*. 1998;40(2–3):273-286.
7. Yao R, Herrera JE, Chen L, Chin Y-HC. Generalized mechanistic framework for ethane dehydrogenation and oxidative dehydrogenation on molybdenum oxide catalysts. *ACS Catal*. 2020;10(12):6952-6968.
8. Jiang X, Sharma L, Fung V, et al. Oxidative dehydrogenation of propane to propylene with soft oxidants via heterogeneous catalysis. *ACS Catal*. 2021;11(4):2182-2234.
9. Liu Y, Twombly A, Dang Y, Mirich A, Suib SL, Deshlahra P. Roles of enhancement of C–H activation and diminution of C–O formation within M1-phase pores in propane selective oxidation. *Chem Cat Chem*. 2021;13(3):882-899.
10. Schlögl R. Concepts in selective oxidation of small alkane molecules. In: Mizuno N, ed. *Modern Heterogeneous Oxidation Catalysis: Design, Reactions and Characterization*. Wiley; 2009:1-42.
11. Gärtner CA, van Veen AC, Lercher JA. Oxidative dehydrogenation of ethane: common principles and mechanistic aspects. *ChemCatChem*. 2013;5(11):3196-3217.
12. Najari S, Saeidi S, Concepcion P, et al. Oxidative dehydrogenation of ethane: catalytic and mechanistic aspects and future trends. *Chem Soc Rev*. 2021;50:4564-4605.
13. Argyle MD, Chen K, Bell AT, Iglesia E. Effect of catalyst structure on oxidative dehydrogenation of ethane and propane on alumina-supported Vanadia. *J Catal*. 2002;208(1):139-149.
14. Chen K, Khodakov A, Yang J, Bell AT, Iglesia E. Isotopic tracer and kinetic studies of oxidative dehydrogenation pathways on vanadium oxide catalysts. *J Catal*. 1999;186(2):325-333.
15. Labinger JA, Bercaw JE. Understanding and exploiting C–H bond activation. *Nature*. 2002;417(6888):507-514.
16. Argyle MD, Chen K, Bell AT, Iglesia E. Ethane oxidative dehydrogenation pathways on vanadium oxide catalysts. *J Phys Chem B*. 2002;106(21):5421-5427.
17. Dai G-L, Liu Z-P, Wang W-N, Lu J, Fan K-N. Oxidative dehydrogenation of ethane over V_2O_5 (001): a periodic density functional theory study. *J Phys Chem C*. 2008;112(10):3719-3725.
18. Rozanska X, Sauer J. Oxidative conversion of C1–C3 alkanes by vanadium oxide catalysts. DFT results and their accuracy. *Int J Quantum Chem*. 2008;108(12):2223-2229.
19. Annamalai L, Ezenwa S, Dang Y, Tan H, Suib SL, Deshlahra P. Comparison of structural and catalytic properties of monometallic Mo and V oxides and M1 phase mixed oxides for oxidative dehydrogenation. *Catal Today*. 2020;368:28-45.
20. Annamalai L, Liu Y, Ezenwa S, Dang Y, Suib SL, Deshlahra P. Influence of tight confinement on selective oxidative dehydrogenation of ethane on MoVTeNb mixed oxides. *ACS Catal*. 2018;8(8):7051-7067.
21. Mars P, Van Krevelen DW. Oxidations carried out by means of vanadium oxide catalysts. *Chem Eng Sci*. 1954;3:41-59.
22. Deshlahra P, Carr RT, Chai S-H, Iglesia E. Mechanistic details and reactivity descriptors in oxidation and acid catalysis of methanol. *ACS Catal*. 2014;5(2):666-682.

23. Iwasaki M, Iglesia E. Mechanistic assessments of NO oxidation turnover rates and active site densities on WO3-promoted CeO2 catalysts. *J Catal*. 2016;342:84-97.
24. Wu Z, Li M, Howe J, Meyer HM III, Overbury SH. Probing defect sites on CeO2 nanocrystals with well-defined surface planes by Raman spectroscopy and O2 adsorption. *Langmuir*. 2010;26(21):16595-16606.
25. Kwon S, Deshlahra P, Iglesia E. Dioxygen activation routes in Mars-van Krevelen redox cycles catalyzed by metal oxides. *J Catal*. 2018;364:228-247.
26. Kwon S, Deshlahra P, Iglesia E. Reactivity and selectivity descriptors of dioxygen activation routes on metal oxides. *J Catal*. 2019;377:692-710.
27. Reynolds MS, Butler A. Oxygen-17 NMR, electronic, and vibrational spectroscopy of transition metal peroxo complexes: correlation with reactivity. *Inorg Chem*. 1996;35(8):2378-2383.
28. Liu J, Mohamed F, Sauer J. Selective oxidation of propene by vanadium oxide monomers supported on silica. *J Catal*. 2014;317:75-82.
29. Rozanska X, Kondratenko EV, Sauer J. Oxidative dehydrogenation of propane: differences between N_2O and O_2 in the reoxidation of reduced Vanadia sites and consequences for selectivity. *J Catal*. 2008;256(1):84-94.
30. Goodrow A, Bell AT. A theoretical investigation of the selective oxidation of methanol to formaldehyde on isolated vanadate species supported on silica. *J Phys Chem C*. 2007;111(40):14753-14761.
31. Cavani F, Trifiro F. Selective oxidation of light alkanes: interaction between the catalyst and the gas phase on different classes of catalytic materials. *Catal Today*. 1999;51(3–4):561-580.
32. Annamalai L, Liu Y, Deshlahra P. Selective C–H bond activation via NOx-mediated generation of strong H-abstractors. *ACS Catal*. 2019;9(11):10324-10338.
33. Leveles L, Seshan K, Lercher J, Lefferts L. Oxidative conversion of propane over lithium-promoted magnesia catalyst: I. Kinetics and mechanism. *J Catal*. 2003;218(2):296-306.
34. Lercher J, Naraschewski F. *Nanostructured Catalysts-Selective Oxidation*. Royal Society of Chemistry; 2011.
35. Gao Y, Neal L, Ding D, et al. Recent advances in intensified ethylene production—a review. *ACS Catal*. 2019;9(9):8592-8621.
36. Takanabe K, Shahid S. Dehydrogenation of ethane to ethylene via radical pathways enhanced by alkali metal based catalyst in oxysteam condition. *AIChE J*. 2017;63(1):105-110.
37. Takanabe K, Khan AM, Tang Y, et al. Integrated in situ characterization of a molten salt catalyst surface: evidence of sodium peroxide and hydroxyl radical formation. *Angew Chem Int Ed*. 2017;56(35):10403-10407.
38. Zalc JM, Green WH, Iglesia E. NOx-mediated homogeneous pathways for the synthesis of formaldehyde from CH_4—O_2 mixtures. *Ind Eng Chem Res*. 2006;45(8):2677-2688.
39. Takanabe K, Iglesia E. Mechanistic aspects and reaction pathways for oxidative coupling of methane on Mn/Na2WO4/SiO2 catalysts. *J Phys Chem C*. 2009;113(23):10131-10145.
40. Skoufa Z, Giannakakis G, Heracleous E, Lemonidou AA. Simulation-aided effective design of a catalytic reactor for ethane oxidative dehydrogenation over NiNbOx. *Catal Today*. 2018;299:102-111.
41. Waku T, Argyle MD, Bell AT, Iglesia E. Effects of O2 concentration on the rate and selectivity in oxidative dehydrogenation of ethane catalyzed by vanadium oxide: implications for O2 staging and membrane reactors. *Ind Eng Chem Res*. 2003;42(22):5462-5466.
42. Frisch M. et al. Gaussian 09 Rev. D.01 [computer program]. Wallingford, CT 2013.
43. Lee C, Yang W, Parr RG. Development of the Colle-Salvetti correlation-energy formula into a functional of the electron density. *Phys Rev B*. 1988;37(2):785-789.
44. Becke AD. A new mixing of Hartree–Fock and local density-functional theories. *J Chem Phys*. 1993;98(2):1372-1377.
45. Schäfer A, Huber C, Ahlrichs R. Fully optimized contracted Gaussian basis sets of triple zeta valence quality for atoms Li to Kr. *J Chem Phys*. 1994;100(8):5829-5835.
46. Weigend F, Ahlrichs R. Balanced basis sets of split valence, triple zeta valence and quadruple zeta valence quality for H to Rn: design and assessment of accuracy. *Phys Chem Chem Phys*. 2005;7(18):3297-3305.
47. Weigend F. Accurate Coulomb-fitting basis sets for H to Rn. *Phys Chem Chem Phys*. 2006;8(9):1057-1065.
48. Grimme S, Ehrlich S, Goerigk L. Effect of the damping function in dispersion corrected density functional theory. *J Comput Chem*. 2011;32(7):1456-1465.
49. McQuarrie D. Chapter 8, Ideal polyatomic gas. In: Rice A. Stuart, ed. University Science Books; 2000:222-223.
50. Sprowl LH, Campbell CT, Arnadottir L. Hindered translator and hindered rotor models for adsorbates: partition functions and entropies. *J Phys Chem C*. 2016;120(18):9719-9731.
51. Campbell CT, Sellers JR. Enthalpies and entropies of adsorption on well-defined oxide surfaces: experimental measurements. *Chem Rev*. 2013;113(6):4106-4135.
52. Susnow RG, Dean AM, Green WH, Peczak P, Broadbelt LJ. Rate-based construction of kinetic models for complex systems. *J Phys Chem A*. 1997;101(20):3731-3740.
53. Gao CW, Allen JW, Green WH, West RH. Reaction mechanism generator: automatic construction of chemical kinetic mechanisms. *Comput Phys Commun*. 2016;203:212-225.
54. Liu M, Grinberg Dana A, Johnson M, et al. *Reaction Mechanism Generator v3. 0: Advances in Automatic Mechanism Generation*. ACS Publications; 2020.
55. Burke MP, Chaos M, Ju Y, Dryer FL, Klippenstein SJ. Comprehensive H2/O2 kinetic model for high-pressure combustion. *Int J Chem Kinet*. 2012;44(7):444-474.
56. Bugler J, Marks B, Mathieu O, et al. An ignition delay time and chemical kinetic modeling study of the pentane isomers. *Combust Flame*. 2016;163:138-156.
57. Hashemi H, Christensen JM, Gersen S, Levinsky H, Klippenstein SJ, Glarborg P. High-pressure oxidation of methane. *Combust Flame*. 2016;172:349-364.
58. Benson SW. *Thermochemical Kinetics*. John Wiley; 1976.
59. Goodwin DG, Moffat HK, Speth RL. *Cantera: An Object-Oriented Software Toolkit for Chemical Kinetics, Thermodynamics, and Transport Processes*. Zenodo; 2009.
60. Bishop DM, Laidler KJ. Symmetry numbers and statistical factors in rate theory. *J Chem Phys*. 1965;42(5):1688-1691.
61. Pollak E, Pechukas P. Symmetry numbers, not statistical factors, should be used in absolute rate theory and in Broensted relations. *J Am Chem Soc*. 1978;100(10):2984-2991.
62. Fernández-Ramos A, Ellingson BA, Meana-Pañeda R, Marques JM, Truhlar DG. Symmetry numbers and chemical reaction rates. *Theor Chem Acc*. 2007;118(4):813-826.
63. Gao X, Bare SR, Weckhuysen BM, Wachs IE. In situ spectroscopic investigation of molecular structures of highly dispersed vanadium oxide on silica under various conditions. *J Phys Chem B*. 1998;102(52):10842-10852.
64. Jaegers NR, Wan C, Hu MY, et al. Investigation of silica-supported vanadium oxide catalysts by high-field 51V magic-angle spinning NMR. *J Phys Chem C*. 2017;121(11):6246-6254.
65. Carrero CA, Keturakis CJ, Orrego A, Schomäcker R, Wachs IE. Anomalous reactivity of supported V 2 O 5 nanoparticles for propane oxidative dehydrogenation: influence of the vanadium oxide precursor. *Dalton Trans*. 2013;42(35):12644-12653.
66. Rozanska X, Fortrie R, Sauer J. Oxidative dehydrogenation of propane by monomeric vanadium oxide sites on silica support. *J Phys Chem C*. 2007;111(16):6041-6050.

67. Rozanska X, Fortrie R, Sauer J. Size-dependent catalytic activity of supported vanadium oxide species: oxidative dehydrogenation of propane. *J Am Chem Soc*. 2014;136(21):7751-7761.
68. Deshlahra P, Iglesia E. Reactivity and selectivity descriptors for the activation of C–H bonds in hydrocarbons and oxygenates on metal oxides. *J Phys Chem C*. 2016;120(30):16741-16760.
69. Fung V, Tao F. Jiang De. Trends of alkane activation on doped cobalt (II, III) oxide from first principles. *Chem Cat Chem*. 2018;10(1):244-249.
70. Liu Y, Annamalai L, Deshlahra P. Effects of lattice O atom coordination and pore confinement on selectivity limitations for ethane oxidative dehydrogenation catalyzed by vanadium-Oxo species. *J Phys Chem C*. 2019;123(46):28168-28191.
71. van den Reijen JE, Versluis WC, Kanungo S, d'Angelo MF, de Jong KP, de Jongh PE. From qualitative to quantitative understanding of support effects on the selectivity in silver catalyzed ethylene epoxidation. *Catal Today*. 2019;338:31-39.
72. Venegas JM, Zhang Z, Agbi TO, McDermott WP, Alexandrova A, Hermans I. Why boron nitride is such a selective catalyst for the oxidative dehydrogenation of propane. *Angew Chem Int Ed*. 2020;59(38):16527-16535.
73. Kaiser E, Wallington T, Andino J. Pressure dependence of the reaction C2H5+ O2. *Chem Phys Lett*. 1990;168(3–4):309-313.
74. Ignatyev IS, Xie Y, Allen WD, III HFS. Mechanism of the C2H5+O2 reaction. *J Chem Phys*. 1997;107(1):141-155.
75. Towns J, Cockerill T, Dahan M, et al. XSEDE: accelerating scientific discovery. *Comput Sci Eng*. 2014;16(5):62-74.

SUPPORTING INFORMATION

Additional supporting information may be found in the online version of the article at the publisher's website.

How to cite this article: Liu Y, McGill CJ, Green WH, Deshlahra P. Effects of surface species and homogeneous reactions on rates and selectivity in ethane oxidation on oxide catalysts. *AIChE J*. 2021;67(12):e17483. doi: 10.1002/aic.17483